MRI-Based Lesion Profiling of Epileptogenic Cortical Malformations

Seok-Jun Hong, Boris C. Bernhardt, Dewi Schrader, Benoit Caldairou, Neda Bernasconi, and Andrea Bernasconi

Neuroimaging of Epilepsy Laboratory, McConnell Brain Imaging Centre, Montreal Neurological Institute and Hospital, McGill University, Montreal, Quebec, Canada
sjhong@bic.mni.mcgill.ca

Abstract. Focal cortical dysplasia (FCD), a malformation of cortical development, is a frequent cause of drug-resistant epilepsy. This lesion is histologically classified into Type-IIA (dyslamination, dysmorphic neurons) and Type-IIB (dyslamination, dysmorphic neurons, and balloon cells). Reliable *in-vivo* identification of lesional subtypes is important for preoperative decision-making and surgical prognostics. We propose a novel multi-modal MRI lesion profiling based on multiple surfaces that systematically sample intra- and subcortical tissue. We applied this framework to histologically-verified FCD. We aggregated features describing morphology, intensity, microstructure, and function from T1-weighted, FLAIR, diffusion, and resting-state functional MRI. We observed alterations across multiple features in FCD Type-IIB, while anomalies in IIA were subtle and mainly restricted to FLAIR intensity and regional functional homogeneity. Anomalies in Type-IIB were seen across all intra- and subcortical levels, whereas those in Type-IIA clustered at the cortico-subcortical interface. A supervised classifier predicted the FCD subtype with 91% accuracy, validating our profiling framework at the individual level.

Keywords: Intracortical, FCD, Multimodal MRI, Histopathological prediction.

1 Introduction

Focal cortical dysplasia (FCD), a highly epileptogenic malformation of cortical development, is a frequent cause of drug-resistant epilepsy in children and adults. Surgical resection of these lesions is the only effective treatment to arrest the seizures.

Histologically, FCD is characterized by cortical dyslamination associated with various intra-cortical cytological anomalies: large dysmorphic neurons typify FCD Type-IIA, while clusters of balloon cells and dysmorphic neurons are characteristic of Type-IIB [1]. In addition to cortical abnormalities, neuronal density is increased in the white matter immediately below the cortical interface. Radiological assessments suggest that these histological subtypes may have diverging morphological and intensity signatures, with Type-IIA being generally more subtle than IIB [1]. Moreover, difficulties to discern lesional boundaries from the surrounding normal cortex, together

N. Navab et al. (Eds.): MICCAI 2015, Part II, LNCS 9350, pp. 501–509, 2015.
DOI: 10.1007/978-3-319-24571-3_60

with a more extended epileptogenic network [2], explain less favorable surgical outcome prospects in FCD Type-IIA compared to type-IIB [3].

Given the irreversible nature of surgery, it is important to predict FCD subtypes *in vivo*. We propose a surface-based multivariate MRI framework that jointly assesses morphology, intensity, diffusion, and functional characteristics, taking advantage of their covariance for improved lesion profiling. To model FCD-related cortical dyslamination and white matter gliosis, we sampled imaging parameters on multiple surfaces at various cortical and subcortical depths. We used a supervised classifier to automatically predict the histological subtype from multiparametric MRI.

2 Methods

Figure 1 summarizes our approach. Each step is detailed in the text below.

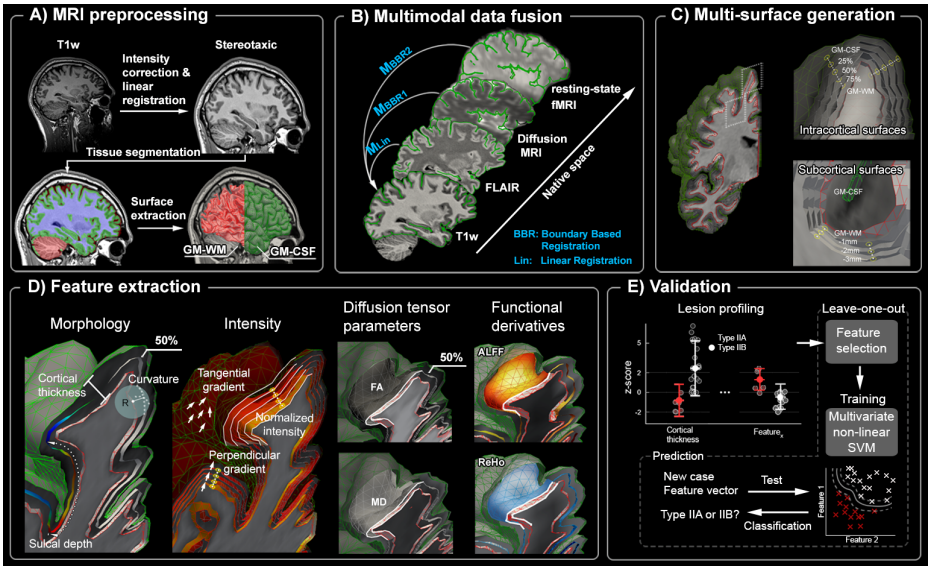

Fig. 1. Flowchart of the proposed method

2.1 MRI Acquisition

Acquisition. Multimodal MRI was acquired on a 3T Siemens TimTrio using a 32-channel head coil. Structural MRI included a 3D T1-weighted (T1w) MPRAGE (TR = 2300ms, TE=2.98ms, FA=9°, FOV=256mm^2, voxel size= 1×1×1mm^3) and fluid-attenuated inversion recovery (FLAIR; TR=5000ms, TE=389 ms, TI=1.8ms, FA=120°, FOV=230mm^2, voxel size=0.9×0.9×0.9mm^3). Diffusion-weighted MRI data were obtained using a 2D-EPI sequence (TR=8400ms, TE=90ms, FA=90°, FOV=256mm^2, voxel size=2×2×2mm^3, 64 directions, b=1000s/mm^2, 1 B0). Resting-state fMRI (rs-fMRI) was acquired using a 2D-BOLD-EPI sequence (TR=2020ms, TE=30ms, FA=90°, FOV=256mm^2, 34 slices, voxel size=4×4×4mm^3, 150 volumes).

2.2 MRI Preprocessing and Multimodal Data Fusion (Fig. 1A, B)

T1w underwent intensity inhomogeneity correction, intensity standardization, linear registration to MNI152 space, as well as classification into white matter (WM), gray matter (GM), and cerebro-spinal fluid (CSF) [4]. GM-WM and GM-CSF surface models were constructed using CLASP, an algorithm relying on intensity and geometric constraints [5]. Notably, as the GM-CSF surface is generated directly from the GM-WM surface, both surfaces have the same number of vertices. Moreover, corresponding vertices on both surfaces can be connected using straight line, a so-called *t-link*. A surface registration based on cortical folding improved inter-subject alignment. After intensity correction, FLAIR data were co-registered to native T1w. Diffusion-weighted data were corrected for motion, eddy currents, and geometric distortions; we obtained fractional anisotropy (FA) and mean diffusivity (MD) using FSL (v5.0; http://fsl.fmrib.ox.ac.uk/fsl/). The rs-fMRI data were corrected for slice-time, motion, geometric distortions, and nuisance signals of WM and CSF. Scrubbing corrected residual motion confounds [6]. Diffusion-weighted MRI and rs-fMRI were co-registered to T1w using boundary-based registration [7].

2.3 Multi-surface Generation (Fig. 1C)

We reconstructed three intracortical surfaces equidistantly positioned between GM-CSF and GM-WM boundaries along the t-link at 25, 50, and 75% thickness. Although these surfaces do not necessarily reflect exact cortical laminae, they capture relative differences along the axis perpendicular to the cortical mantle. A set of subcortical surfaces was constructed to probe intensity and diffusion parameters in the WM immediately below the cortex; for each individual, a Laplacian deformation field running from the GM-WM interface towards the ventricles guided subcortical surface placement. A Laplacian field represents a map of smoothly increasing equipotential surfaces between two boundaries $\boldsymbol{S}_0$ and $\boldsymbol{M}$ and guarantees a similar triangular topology throughout the deformation. Let ψ denote the electrostatic potential at equilibrium of some quantity. Then, the net flux of ψ through the boundary S of a control volume V is defined as following:

$$\int \nabla\psi \bullet \mathbf{n}\, dS = 0 \tag{1}$$

where dS is the area of an infinitesimal surface element on the boundary and $\mathbf{n}$ is a surface normal vector. In Cartesian coordinates, Laplace's equation is expressed as:

$$\Delta\psi = \nabla^2\psi = \frac{\partial\psi}{\partial x^2} + \frac{\partial\psi}{\partial y^2} + \frac{\partial\psi}{\partial z^2} \tag{2}$$

Given boundary conditions as $\psi_1 = \boldsymbol{S}_0$ (GM-WM interface) and $\psi_2 = \boldsymbol{M}$ (ventricle), solving **Eq. (2)** results in a smooth transition of equipotentials within V. Intervals

between subcortical surfaces were adapted to the native resolution of each modality (T1/FLAIR: 1/0.9mm and diffusion: 2mm). Please note that the use of more widely-spaced surfaces for the sampling of diffusion parameters minimized residual misregistration errors due to EPI-specific image distortions.

2.4 Surface-Based Feature Extraction

Features were extracted in the native space of the respective modalities to minimize interpolation. To control for regional feature variability after surface smoothing (FWHM=5mm), measures in a given patient were z-transformed at each vertex with respect to the corresponding distribution in controls (*see below*).

Intensity and Texture. To assess lesional intensity, we calculated the difference between the T1w (and FLAIR) intensity at a given voxel and averaged GM-WM boundary intensity, and normalized it by the mode of the intensity histogram. These *normalized intensity* values were mapped to surfaces using a linear interpolation. To model intracortical dyslamination, we computed intensity gradients in perpendicular and tangential direction with respect to cortical surface geometry. *Perpendicular gradient* was computed as the difference in intensity between corresponding vertices above and below a vertex v_i on neighboring surfaces, divided by their distance. *Tangential gradient* was computed along each surface, by averaging differences of intensity of the surface-neighbors of v_i, divided by the mean distance from neighboring vertices. We did not sample intensity at the outermost GM-CSF surface to avoid large CSF partial volume effects *(PVE_{CSF}).* At other surfaces, PVE_{CSF} was corrected similar to a previous approach [8]. In brief, we automatically estimated PVE_{GM} and PVE_{CSF} on T1w- and FLAIR-MRI [9] and mapped these values to intra-cortical surfaces. Observed intensity (I) at v_i was modeled as: $I=PVE_{GM}\times I_{GM}(v_i)+PVE_{CSF}(v_i)\times I_{CSF}(v_i)$, where I_{GM}/ I_{CSF} are pure intensities of GM/CSF. $I_{CSF}(v_i)$ was computed by averaging intensity of neighboring voxels considered 'pure' CSF (voxels with PVE_{CSF}=1, within a radius of 10 mm around v_i). Solving the equation provides the remaining term RI_{GM} (*i.e.*, the hypothetical CSF–free GM intensity) at each vertex.

Morphology. Cortical thickness was calculated as the Euclidean distance between corresponding vertices on the GM-WM and GM-CSF surfaces [5]. As small FCD lesions are often located at the bottom of a sulcus [10], we computed sulcal depth by overlaying a brain hull on the GM-CSF boundary to detect gyral crowns; for a given vertex, sulcal depth was computed as the shortest geodesic distance from a crown.

Diffusion tensor parameters. FA and MD are proxies for fiber architecture and microstructure. Due to lower resolution, we sampled FA and MD at the 50% intra-cortical, the GM-WM boundary and subcortical surfaces lying at 2 and 4 mm depth.

Functional MRI metrics. We calculated two voxel-wise markers of local functional integrity: amplitude of low frequency fluctuations (ALFF) and regional homogeneity (ReHo) [11]. While ALFF is computed as the total time-series power in the 0.01-0.08 Hz band, ReHo quantifies local time-series variance within a 27-voxel-neighborhood. Functional features were sampled on the 50% intra-cortical surface.

3 Experiment and Results

3.1 Subjects

We studied 33 consecutive patients (17 males; mean±SD age=28±10 years) with histologically-proven FCD Type-II (9 IIA, 24 IIB) admitted to our Hospital for the investigation of focal epilepsy. The presurgical workup included a neurologic examination, assessment of seizure history, neuroimaging, and video-EEG telemetry. The FCD subgroups did not show statistical differences in age, sex, age at onset, disease duration, and focus lateralization. As control group, we studied 41 age- and sex-matched healthy individuals (21 males; mean±SD age=30±7 years).

3.2 Lesion Profiling

Manual Segmentation. Two trained raters independently segmented FCD lesions on co-registered T1w and FLAIR images; their consensus volume label was intersected with the surface models, thereby generating surface-based lesion labels.

Lesion Profiling. For each patient, z-scores of a given feature **(2.3)** were averaged across all intracortical/subcortical vertices within the consensus label to obtain a global lesion profile. Global profiling was complemented by systematic analysis of feature variations across individual intracortical and subcortical surfaces.

Statistical Analysis. Using two-sample Student's t-tests, we compared global and multi-surface profiles between each patient group (*i.e.*, FCD Type-IIA and IIB) to controls, and patient cohorts to each other. We utilized the Benjamini-Hochberg procedure to control the false discovery rate (FDR) to be below q=0.05 [12].

3.3 Machine-Learning Prediction of Histological Subtypes

A support vector machine (SVM) with a polynomial 3rd-order kernel was used to automatically predict the histological FCD subtype in individual patients. Using a leave-one-out cross-validation scheme, we performed a forward-sequential feature selection, trained the classifier, and evaluated prediction performance. The forward-sequential procedure added features to an empty set until classification rates were not further improved. We evaluated the *box-constraint* parameter C, a penalty for non-separable samples, across C=0.1-1000. As accuracies were stable across the entire range, C was set to the default of 1. We visualized classification results through multidimensional scaling. SVM performance was evaluated for three different feature categories: *i)* Global features from single modalities (*e.g.,* only features derived from FLAIR); *ii)* Global multi-modal features (*e.g.,* combinations of features derived from T1w, FLAIR, DWI, and rs-fMRI); *iii)* multimodal and multi-surface (intracortical and subcortical) features.

3.4 Results

Global Lesion Profiling (**Fig. 2**). Compared to controls, FCD Type-IIB was associated with a wide range of morphological and intensity anomalies (*increased* cortical thickness, sulcal depth, intracortical/subcortical FLAIR intensity, subcortical MD; *decreased* perpendicular T1w/FLAIR gradient, tangential T1w gradient), while anomalies in Type-IIA were restricted to increased FLAIR intensity (q_{FDR}=0.05). Directly comparing both FCD cohorts revealed increased FLAIR intensity, cortical thickness, sulcal depth, and decreased vertical T1w gradient in Type-IIB (q_{FDR}<0.05). Functional profiling revealed decreased ALFF and ReHo in Type-IIB compared to controls (q_{FDR} <0.03). Type-IIA, on the other hand, showed marginally increased ReHo compared to controls (q_{FDR}<0.07). Direct subtype comparisons confirmed significant decreases across both features in Type-IIB (q_{FDR} <0.01).

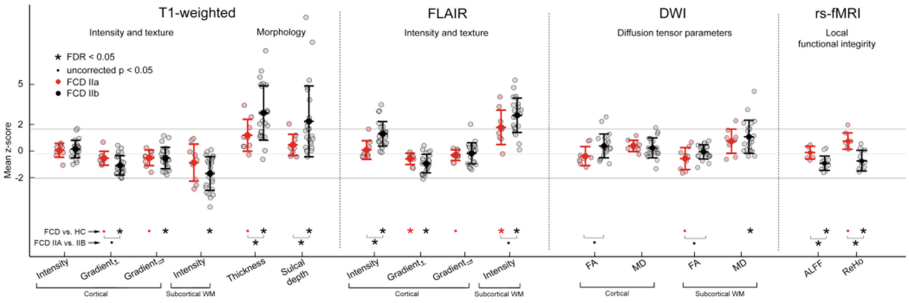

Fig. 2. Global lesion profiling. Graphs show feature z-scores *w.r.t.* controls in FCD Type-IIA (*red*) and IIB (*black*). Significant differences from controls and between patient groups are indicated by asterisks (q_{FDR}<0.05), trends are displayed as small circles (p<0.05).

Multi-Surface Profiling (**Fig. 3**). Multi-surface analysis revealed marked abnormalities across virtually all intracortical levels in Type-IIB (increased FLAIR intensity, decreased vertical T1w/FLAIR gradient), while alterations in IIA were proximal to the GM-WM interface (decreased T1w/FLAIR gradients). Likewise, WM alterations in Type-IIB were found across all subcortical surfaces (decreased T1w intensity, increased FLAIR intensity and MD; q_{FDR}<0.02). Type-IIA presented with FLAIR intensity increases in subcortical WM at 1 mm depth (q_{FDR}<0.02). Direct FCD cohort comparisons revealed increased FLAIR intensity in Type-IIB relative to IIA across all intracortical and the 1 mm deep subcortical WM surfaces (q_{FDR}=0.03). Conversely, FA was reduced in Type-IIA relative to IIB (q_{FDR}=0.05).

Prediction of Histological Subtypes (**Fig. 4**). An SVM trained on multi-surface features derived from structural and functional modalities accurately predicted the FCD subtype in 91% (21/23, missing one IIA and one IIB), outperforming SVMs trained on single modalities (52-70%) or classifiers using only global features (83%). We repeated the analysis with a 10-fold cross-validation (100 times) and addressed unbalanced group sizes by adding 'bagging' (100 times; randomly selecting equal numbers of training cases from each subtype). Using this scheme, we observed a slightly lower, but still excellent overall performance (87% accuracy, sensitivity: 89%, specificity: 85%). Permutation tests with 10,000 iterations confirmed that the

achieved accuracy exceeded chance-level ($p<0.001$). A mean±SD=3±1 features were selected across leave-one-out iterations at optimal accuracy. In order of contribution, these were: ReHo, T1w-vertical gradient (75% depth), FLAIR intensity (25 and 50% depth), cortical thickness, subcortical FA (2mm depth), and ALFF.

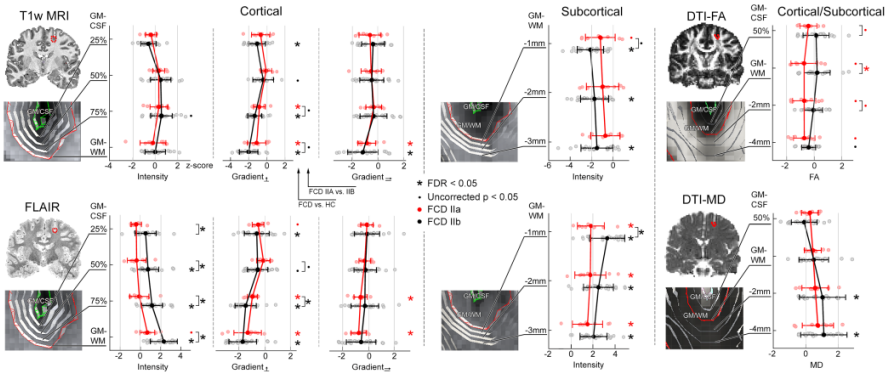

Fig. 3. Plots display multi-surface lesion profiles at various intra-/subcortical depths. Circles indicate FCD subtypes (*red/black* for Type IIA/IIB). For a given lesion, feature values are z-normalized relative to controls and averaged within the consensus label. Inter-surface spacing is based on the relative native imaging resolution.

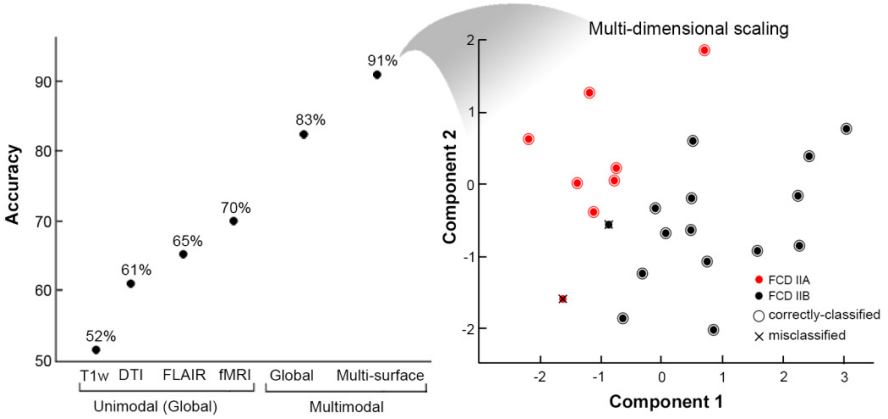

Fig. 4. MRI-based FCD subtype prediction across feature combinations *(left)*. For display purposes, the high dimensional feature space was projected to 2D using multi-dimensional scaling *(right)*. Circles indicate FCD subtypes (*red/black* for Type IIA/IIB). Correctly classified cases are surrounded by a *circle*, misclassified cases are marked by x.

4 Discussion

Global lesion profiling showed that cortical thickening, T1w hypointensity, FLAIR hyperintensity, and increased sulcal depth are associated with FCD Type-IIB lesions,

while Type-IIA has a more subtle impact on neuroimaging markers. The subtype divergence was refined by the multi-surface analysis, revealing marked intensity and gradient abnormalities in IIB across all intracortical surfaces; conversely, anomalies in IIA were located proximal to the GM-WM interface. The selective alteration of upper cortical surfaces in IIB relate to the preferential location of immature progenitors, including balloon cells, in superficial laminae [13].

Subtypes also diverged with regards to functional metrics. Our finding of decreased ReHo in FCD Type-IIB may indicate abnormal intracortical signal integration that possibly results from the presence of balloon cell clusters acting as barriers to cortico-cortical connections [2]. Conversely, increased ReHo in Type-IIA may reflect enhanced functional synchronization due to excessive activation of dysmorphic neurons.

Few previous studies modeled FCD lesions, either using voxel- [14] or surface-based analysis [10, 15]. Feature modeling was generally limited to T1w features. Moreover, no work attempted to differentiate histological subtypes. The novelty of our work resides in: i) modeling cortical dyslamination via a multi-surface approach; ii) multicontrast MRI features targeting both the GM and the subcortical WM, iii) probing functional integrity; iv) predicting FCD subtypes through machine-learning. In the latter machine-learning experiment, we could validate our profiling approach by predicting histological subtypes with excellent (91%) accuracy. Our results emphasize the utility of integrating metrics of structure and function to dissociate neuroimaging signatures of surgically remediable epileptogenic malformations, with potential application to various neurological conditions in which disease staging is important, such as neurodegenerative disorders, multiple sclerosis, and tumors.

Reference

1. Blumcke, I., et al.: The clinicopathologic spectrum of focal cortical dysplasias: a consensus classification proposed by an ad hoc Task Force of the ILAE Diagnostic Methods Commission. Epilepsia 52(1), 158–174 (2011)
2. Boonyapisit, K., et al.: Epileptogenicity of focal malformations due to abnormal cortical development: Direct electrocorticographic histopathologic correlations. Epilepsia 44(1), 69–76 (2003)
3. Tassi, L., et al.: Electroclinical, MRI and neuropathological study of 10 patients with nodular heterotopia, with surgical outcomes. Brain 128(Pt. 2), 321–337 (2005)
4. Zijdenbos, A.P., Forghani, R., Evans, A.C.: Automatic "pipeline" analysis of 3-D MRI data for clinical trials: application to multiple sclerosis. IEEE Trans. Med. Imaging 21(10), 1280–1291 (2002)
5. Kim, J.S., et al.: Automated 3-D extraction and evaluation of the inner and outer cortical surfaces using a Laplacian map and partial volume effect classification. Neuroimage 27(1), 210–221 (2005)
6. Power, J.D., et al.: Spurious but systematic correlations in functional connectivity MRI networks arise from subject motion. Neuroimage 59(3), 2142–2154 (2012)
7. Greve, D.N., Fischl, B.: Accurate and robust brain image alignment using boundary-based registration. Neuroimage 48(1), 63–72 (2009)

8. Shafee, R., Buckner, R.L., Fischl, B.: Gray matter myelination of 1555 human brains using partial volume corrected MRI images. Neuroimage 105, 473–485 (2015)
9. Tohka, J., Zijdenbos, A., Evans, A.: Fast and robust parameter estimation for statistical partial volume models in brain MRI. Neuroimage 23(1), 84–97 (2004)
10. Besson, P., et al.: Small focal cortical dysplasia lesions are located at the bottom of a deep sulcus. Brain 131(Pt. 12), 3246–3255 (2008)
11. Yuan, R., et al.: Regional homogeneity of resting-state fMRI contributes to both neurovascular and task activation variations. Magn. Reson. Imaging 31(9), 1492–1500 (2013)
12. Benjamini, Y., Hochberg, Y.: Controlling the false discovery rate: a practical and powerful approach to multiple testing. Journal of the Royal Statistical Society. Series B (Methodological), 289–300 (1995)
13. Sakakibara, T., et al.: Delayed maturation and differentiation of neurons in focal cortical dysplasia with the transmantle sign: analysis of layer-specific marker expression. J. Neuropathol. Exp. Neurol. 71(8), 741–749 (2012)
14. Colliot, O., et al.: In vivo profiling of focal cortical dysplasia on high-resolution MRI with computational models. Epilepsia 47(1), 134–142 (2006)
15. Thesen, T., et al.: Detection of epileptogenic cortical malformations with surface-based MRI morphometry. PLoS One 6(2), e16430 (2011)